Supplementary Information

Two-Dimensional Nanoplatelet Superlattices Overcoming Intrinsic Light Outcoupling Efficiency Limit in Perovskite Quantum Dot Light-Emitting Diodes

Sudhir Kumar[1†], Tommaso Marcato[1†], Frank Krumeich[2], Yen-Ting Li[3,4], Yu-Cheng Chiu[3], and Chih-Jen Shih[1*]

[1]Institute for Chemical and Bioengineering, ETH Zürich, 8093 Zürich, Switzerland

[2]Laboratory of Inorganic Chemistry, ETH Zürich, 8093 Zürich, Switzerland

[3]Department of Chemical Engineering, National Taiwan University of Science and Technology, Taipei 10607, Taiwan.

[4]National Synchrotron Radiation Research Center, Hsinchu 30076, Taiwan.

[†]Authors contributed equally.

*All to whom all correspondence should be addressed. Email: chih-jen.shih@chem.ethz.ch

1. Methods

1.1 Perovskite band structure

In first approximation, lead trihalide perovskite nanocrystals are modelled as cubic semiconductors with the octahedral symmetry (the O_h point group), where the bandgap occurs at the R point of the Brillouin zone, isomorphic to the Γ point. The six fold conduction and twofold valence bands are contributed from the Pb 6p and halogen 4p orbitals, such that the former possesses p-like (Γ_4^-) symmetry, and the latter s-like (Γ_1^+) symmetry[1].

The symmetry of Bloch states dictates the polarization selection rules for spontaneous emission. We consider as the initial state of the system possessing an electron in the excited conduction band state u_{ck} with momentum k and the electromagnetic field in its vacuum state, i.e. $|u_{ck}; 0\rangle$. The final state has the electron relaxed in the valence band upon emission of a photon of mode j, i.e.$|u_{vk'}; 1_j\rangle$. The probability for the emission of photons of polarization **e** per unit time and per unit solid angle Ω in the direction (θ, ϕ) is given by the Fermi's golden rule[2]:

$$\frac{d\Gamma}{d\Omega}(\theta,\phi) = \frac{2\pi}{\hbar}\,|\langle u_{vk'};\, 1_j \mid \hat{H}_I|u_{ck};\, 0\rangle|^2 \rho(\theta,\phi,E_g = \hbar\omega_j) \qquad (1)$$

where $\hat{H}_I = -\frac{e}{m}\sqrt{\frac{\hbar}{2\epsilon\omega L^3}}(\hat{p}\cdot e)(\hat{a}_j + \hat{a}_j^{\dagger}))$ is the field-matter interaction Hamiltonian where ω_j is angular frequency of the emitted photon L^3 is the field quantization volume, $\hat{p}$ is the momentum operator and $\hat{a}_j, \hat{a}_j$ are respectively the electromagnetic field annihilation and creation operators. $\rho(\theta,\phi,E_g = \hbar\omega_j)$ represents the density of one-photon states of energy equal to the bandgap energy E_g propagating in the direction (θ, ϕ). Accordingly, the polarization of the emitted photons together with the angular radiation pattern are determined by the matrix elements of the operator $\hat{p}$.e. In the following derivations notation from atomic orbitals will be borrowed to label the Bloch states in p-like and s-like bands. As an example |Z⟩ will denote the Block state in the p-like conduction band of orbital angular momentum (l = 1, m_l = 0) given that its spatial symmetry can be described by the same spherical harmonic basis function ($Y_1^0\,(\theta,\phi)$) as a p_z atomic orbital. Similarly, |X⟩ and |Y⟩ denote the remaining states in the conduction band and |S⟩ the valence band states. If we then apply Eq. 1 to a transition between the initial state |Z⟩ and a final state |S⟩ and considering that ⟨S|$\hat{p}_z$|X⟩ = ⟨S|$\hat{p}_z$|Y ⟩ = 0 by symmetry[2]:

$$\frac{d\Gamma}{d\Omega}(\theta,\phi) = \frac{e^2\omega}{8\pi^2\epsilon_0 m_e^2\hbar c^3}\,|\langle S|\hat{p}_z|Z\rangle|^2 sin^2\,\theta \qquad (2)$$

from which we see that the radiation pattern is the same as that of a classical electric dipole oscillating in the z direction. Similarly it can be shown that spontaneous emission from p_x and p_y orbitals is the same of an oscillating electric dipole rotating in the xy plane, i.e. circularly polarized light $\sigma^{\pm}$ in the z direction.

Next, the spin-orbit interaction leads to the splitting of the conduction band states into a fourfold Γ_8^- state and a two fold Γ_6^-. On the other hand, the valance band states, which have zero angular momentum, are not affected and transform as the Γ_6^+ representation[1,3].

Once the spin-orbit interaction is included, the orbital angular momentum is not anymore a good quantum number to label the states so we need to use the total angular momentum and its z projection, i.e. |J, J_z⟩. Diagonalizing the Hamiltonian leads to the following Bloch states[4]: for Γ_8^- states (J = 3/2)

$$|3/2,3/2\rangle = -\frac{1}{\sqrt{2}}(|X\rangle + i|Y\rangle)|\uparrow\rangle \qquad |3/2,-3/2\rangle = \frac{1}{\sqrt{2}}(|X\rangle - i|Y\rangle)|\downarrow\rangle$$

$$|3/2,1/2\rangle = -\frac{1}{\sqrt{6}}(|X\rangle + i|Y\rangle)|\downarrow\rangle + \sqrt{\frac{2}{3}}|Z\rangle|\uparrow\rangle \qquad |3/2,-1/2\rangle = \frac{1}{\sqrt{6}}(|X\rangle - i|Y\rangle)|\uparrow\rangle + \sqrt{\frac{2}{3}}|Z\rangle|\downarrow\rangle$$

and for Γ_6^- states (J = 1/2)

$$|1/2,1/2\rangle = -\frac{1}{\sqrt{3}}(|Z\rangle|\uparrow\rangle + (|X\rangle + i|Y\rangle)|\downarrow\rangle) \qquad |1/2,-1/2\rangle = \frac{1}{\sqrt{3}}(|Z\rangle|\downarrow\rangle - (|X\rangle - i|Y\rangle)|\uparrow\rangle)$$

A good description of the band edge can be obtained by considering only the Γ_6^+ and Γ_6^- states. We notice the latter contains a linear combination of the |X⟩, |Y ⟩, |Z⟩ Bloch states. Following our earlier discussion about Eq. 2, we expect spontaneous emission from optical transitions at the R point to be isotropic in halide perovskites.

In semiconductor nanocrystals (NCs), the quantum confinement leads to strong excitonic characteristics near the band edge. Excitons are two-body bound states of the conduction band electron and the valance band hole coupled via the Coulomb interaction. The wave function follows $\Psi^{exc} = \chi(\mathrm{r_e}, \mathrm{r_h})|\Phi\rangle$, where $\chi(\mathrm{r_e}, \mathrm{r_h})$ is the exciton envelope function and $|\Phi\rangle$ is suitable symmetric or asymmetric linear combination of the Bloch states of the original carriers. Our earlier results do not change by the introduction of excited states. The envelope function varies slowly in the unit cell and it can be factored out in the expression of the matrix elements of the momentum operators. Hence, the symmetry of the original bulk Bloch states remain to control the polarization selection rules.

The four Γ_6^+ and Γ_6^- states are thus combined into four exciton states. These are not all degenerate but they're split by electron-hole exchange interaction into an optically passive singlet Γ_1^- exciton and a bright triplet Γ_4^- exciton[1,3]. Given the composition of the latter in terms of single particle Bloch states and its symmetry, we still conclude that the spontaneous emission is isotropic in cubic lead halide perovskite NCs.

Accordingly, the perovskite radiation behavior appears to be distinct from the conventional zinc blend (ZB) nanocrystals and nanoplatelets (NPLs), e.g. CdSe NPLs. In these crystals, the symmetry of conduction and valence bands is reversed, *p*-like for the valence band and *s*-like for the conduction band, such that the valence band maximum (VBM) is composed of J=3/2 states. At the VBM, |3/2, ±3/2⟩ and |3/2, ±1/2⟩ states, or namely, the heavy-hole (hh) and light-hole (lh) states, respectively, have very different effective masses and thus different quantum confinement energies. In quantum dots and NPLs the band edge exciton is almost exclusively composed of heavy-hole states. These states are linear combinations of |X⟩ and |Y⟩ Bloch states, which form a bright plane and emits anisotropically[5]. In NPLs, where the bright plane coincides with the platelet plane, the emission is anisotropic and directed, because the radiative recombination comes from the in-plane dipoles.

1.2 Anisotropic dielectric confinement

The quantum-mechanical analysis presented earlier, however, did not take into account the effect of dielectric anisotropy, which modulates the electric field experienced by the dipoles generated in individual NCs.

Consider a perovskite NC of dielectric constant ϵ_{NC} which is embedded into a medium of dielectric constant ϵ_m under a uniform electric field **E**. The electric field induces the polarization of the NC, resulting in a local electric field, $E^{loc} = -\nabla_{\phi^{loc}}$ where ϕ^{loc} is the local electric potential. Assuming there are no free carriers residing in the domain considered, the electric potential obeys Laplace equation $\nabla^2_{\phi} = 0$. A solution can then be explicitly related to the external field and be written as

$$E_i^{loc} = f_i(\tilde{\epsilon}, \alpha)E_i \tag{3}$$

where the subscript i = x, y, z coordinates, $\tilde{\epsilon} = \epsilon_{NC}/\epsilon_m$ is the dielectric contrast and α is a geometric anisotropy factor, e.g. the aspect ratio (AR). The solutions for spheroids and square cuboids are discussed as follows.

1.2.1 Spheroids

Consider an ellipsoidal with its semi-axes a, b, and c aligned along the x, y, and z axes, respectively. When $a = b$ (spheroids), the Laplace equation had analytical solutions, which yield.[5-9]

$$f_i = \frac{1}{1+L_i(\tilde{\epsilon}-1)} \tag{4}$$

where L_i are the depolarization factors

$$L_z = \begin{cases} \frac{1-\zeta^2}{2\zeta^3}\left(ln\frac{1+\zeta}{1-\zeta} - 2\zeta\right), & if\ a = b < c\ (prolate) \\ \frac{1+\zeta^2}{\zeta^3}(\zeta - arctan\,\zeta), & if\ c < a = b\ (oblate) \end{cases} \tag{5}$$

$$L_x = L_y = \frac{1 - L_Z}{2}$$

where $\zeta = \sqrt{|1 - a^2/c^2|} = \sqrt{|1 - AR^2|}$. The local field factors for the spheroids are plotted in Fig. 1 as a function of AR (solid curves). The dielectric contrast relevant was estimated using the experimental high frequency $\epsilon_\infty = 4.7$[10-12] for bulk $MAPbBr_3$ and the dielectric constant of oleic acid (2.129)[5] for the alkyl ligand shell.

1.2.2 Cuboids

Consider a cuboidal NC with dimensions of a, b, and c in parallel to x, y, and z directions. When $a = b$ (square cuboids), $f_x = f_y$ and there is only one geometric factor AR = a/c The Laplace equation was solved numerically using the commercial finite element package COMSOL Multiphysics. In each simulation, a square cuboid of given AR was embedded in a uniform dielectric medium and placed between a parallel plate capacitor, which was then biased at 1V to ensure a uniform external electric field. Following eq. 3, the local field factor f_i for a given shape was determined by calculating the local

electric field at the center of mass of NC, E_i^{loc}. Accordingly, the calculated $f_{x,y}$ and f_z as a function of AR are shown in Fig. S1 (empty circles).

Fig. S1 reveals that when AR ≤ 1, the solutions for spheroids and square cuboids are nearly identical. The deviation becomes more significant at intermediate ARs, between 2 to 10, but 3 converges again for AR > 10. We therefore deduce that for the two geometric limits, AR → 0 (rod) and AR → ∞ (disk), the spheroid solutions are asymptotic to those for square cuboids, which are analytically given by

$$\lim_{AR\to 0} f_{x,y} = \frac{2}{1+\tilde{\epsilon}}$$

$$\lim_{AR\to 0} f_z = 1 \qquad (6)$$

$$\lim_{AR\to \infty} f_{x,y} = 1$$

$$\lim_{AR\to \infty} f_z = \frac{1}{\tilde{\epsilon}} \qquad (7)$$

The model, as presented above, describes optical absorption in NCs in the visible range. As a matter of fact, the analysis is valid in the long wavelength approximation, in which the NC characteristic length is significantly smaller than the radiation wavelength $L \ll \frac{\lambda}{2\pi n_m}$. In this approximation electrostatic models holds also in the electrodynamic regime where static fields and permanent dipoles are replaced by frequency dependent fields and oscillating dipoles. The difference of the local field factors along different spheroid and cuboid axes accounts for the experimental observed anisotropy in light absorption by semiconductor NCs. The local field factors arise also in the solution of the reciprocal problem, which models light emission. Considering an electric dipole of moment **d** placed in the center of mass NC, the electric field experienced outside of the NC would be rescaled, effectively identical to the case of placing a dipole of moment $d_i' = f_i d_i$ in the uniform dielectric medium[5,13,14]. Clearly, as shown in Fig. S1, for square platelets (AR > 1), the electric-field screening in the out-of-plane (OP, *z*) direction becomes increasingly stronger than that in the in-plane (IP, *x*-*y*) direction. Consequently, the radiation from an OP dipole is considerably suppressed as compared to an IP dipole. In other words, the effect of dielectric anisotropy would be effectively identical to the change of IP dipole ratio, Θ_{IP}, given by

$$\Theta_{IP} = \frac{d_{IP}}{d_{IP}-d_{OP}} = \frac{2f_x}{2f_x-f_z} \qquad (8)$$

where $d_{IP,OP}$ are IP and OP dipole moments, respectively. Note that when $f_x = f_z$, $\Theta_{IP} = 2/3$, analogous to the case of random dipole orientation in an uniform dielectric medium[5]. Moreover, following Eq. S6-7, for the two geometric limits of rods and disks, ΘIP are given by

$$\lim_{AR\to 0} \Theta_{IP} = \frac{4}{5+\tilde{\epsilon}} \qquad (9)$$

$$\lim_{AR\to\infty} \Theta_{IP} = \frac{2\tilde{\epsilon}}{2\tilde{\epsilon}+1}$$

For the dielectric constants considered here ($\epsilon_{NC} = 4.7$ and $\epsilon_m = 2.129$), we find that the effect of dielectric anisotropy can increase Θ_{IP} up to 0.82 for AR $\rightarrow \infty$. Despite the isotropic nature of halide perovskite electronic structure, the polarization response of anisotropic nanostructures paves to way to achieve directed emission even in halide perovskite thick NPLs.

1.3 Radiative rate in semiconductor nanocrystals

The physical picture presented above is also reflected in the quantum-mechanical behavior of dipoles. The spontaneous emission rate, or the radiative rate, for a given dipole in a semiconductor NC can be expressed as follows[3,7]:

$$\Gamma = \frac{e^2\omega}{3\pi\epsilon_0 m_e^2 \hbar c^3} n_m |f|^2 \hat{p}_i^2 f \qquad (10)$$

where f is the local field factor, nm is the refractive index of the medium and $\hat{p}$ if is the transition dipole moment. Accordingly, in a spheroid or a square cuboid, the radiative rates resulting from IP and OP dipoles, Γ_{IP} and Γ_{OP}, are given by

$$\Gamma_{IP} = \frac{e^2\omega}{3\pi\epsilon_0 m_e^2 \hbar c^3} n_m |f_x|^2 \hat{p}_i^2 f \qquad (11)$$

$$\Gamma_{OP} = \frac{e^2\omega}{3\pi\epsilon_0 m_e^2 \hbar c^3} n_m |f_z|^2 \hat{p}_i^2 f$$

and since $f_z < f_x$ for AR > 1, it appears that in a square platelet or a oblate spheroid, the radiation of out of plane dipoles is inhibited. Together with our findings in Section S1.2-1.3, we point out that although the perovskite quantum-mechanical transition at the R point is ”electronically” isotropic, the effect of dielectric anisotropy at the continuum level could considerably influence the radiation pattern generated from its NC. By engineering the perovskite NC shape and orientation with respect to the substrate, in principle, we anticipate that the light outcoupling efficiency can be enhanced.

1.4 Role of quantum confinement and exciton fine structure

The model, as presented in this text, is expected to be valid for NCs in the weak confinement regime when the characteristic length of the NC is significantly bigger than the bulk Bohr radius. We predict such systems to be affected only by the anisotropic dielectric confinement effect which sets an upper bound of 0.82 to the IP dipole ratio Θ_{IP}. However, a Θ_{IP} of 0.85 has been experimentally observed for $MAPbBr_3$ NPLs, even in thick assembled films[15]. We explain this apparent breakdown of our model by highlighting to additional factors that are expected to play a significant role in strongly quantum confined systems. First, we believe the assumption of the isotropic nature of the band edge electronic structure might not hold till the monolayer limit.

As described in Sec. S1.1, the band edge of $MAPbBr_3$ does not occur at the **k** = 0 point. Despite the fact that the R point is isomorphic to Γ, it has a non-zero component of the crystal momentum into the quantization direction k_z. As k_z is not a good quantum number in the strong quantum confinement limit, a projection of the Bloch states onto the M point of the Brillouin zone is predicted and confirmed by DFT[15]. As the M point has planar D_{4h}, we expect an increase of the IP dipole ratio over the dielectric confinement upper bound in the monolayer limit. A second factor is the internal ordering of the excitonic states, i.e. the exciton fine structure. As derived in Sec. S1.1, the optically active exciton state is an isotropic triplet. However, if the NCs has a low symmetry orthorhombic or tetragonal unit cell structure, the triplet degeneracy can be lifted and the three linear dipole states can be separated and in energy and spectrally resolved[3,16]. Since the fine structure splitting are controlled by the exchange interaction which is very sensitive to NC shape, halide perovskite nanostructures of orthorhombic and tetragonal unit cell symmetry can also break the dielectric confinement limit[16,17].

Nevertheless, given that the NCs explored in this work are only weakly confined and maintain cubic symmetry, engineering the anisotropic dielectric confinement through NC shape is predicted to be the only strategy to increase Θ_{IP} by combining it with ordered assembly in the thin film processing.

2. Characteristics of lead halide perovskite NPLs

2.1 Photophysical characteristics

Figure S2 shows photophysical properties of LHP NPLs having a stoichiometric composition of $FA_{0.5}MA_{0.5}PbBr_3$ passivated with the DA ligand. The absorption (Abs) and PL spectra of spin-coated thin films of LHP "thick" NPLs on glass substrate are plotted as a function of wavelength. The thin-film PL spectrum of DA capped NPLs shows a peak emission at 528±1 nm with a narrow full width half maximum (fwhm) of 22.8 nm, while colloidal dispersion of NPL shows an emission maxima at 528±0.9 nm (fwhm = 22.7 nm) and a η_{PL} of 86.2% at an excitation wavelength (λ_{ext}) of 350 nm. Most interestingly, the η_{PL} of DA capped NPL thin-film reaches almost 100% at λ_{ext} of 350 nm. Upon varying the λ_{ext} between 350 and 500 nm with an interval of 10 nm, the NPL thin-film on glass substrate shows the η_{PL} of 95±5% over the entire excitation range (Fig. S6). The η_{PL} of the NPL thin-films on the cross-linking X-F6TAPC and conventional Poly-TPD layers were also investigated to understand the role of underneath hole transporting layer. On the one hand, the η_{PL}, 95.3%, of NPL thin film remained almost unaffected on the X-F6-TAPC layer. On the other hand, the η_{PL} value, 45%, dramatically suppressed upon spin-casting on top of the Poly-TPD layer. Moreover, the NPL thin-film on the Poly-TPD layer shows notably lower η_{PL} between 350 and 420 nm excitation range due to strong absorption of excitation photons through poly-TPD layer (see Fig. S6 and 8). Moreover, we also observed a notable drop in the average exciton lifetime (τ_{avg}), 44.2 ns, in the NPL thin-film spin-casted on the Poly-TPD layer (Table S1). Undesirable quenching in the η_{PL} and reduced τ_{avg} of NPL thin-film on the Poly-TPD can be

attributed to parasitic emission that induce a non-radiative exciton decay channel (Fig. S6-7). On the contrary, the τ_{avg} = 50 ns in the NPL thin-film on the X-F6-TAPC remain identical with the thin-film sample on bare glass substrate (51.1 ns) (Fig. S9). Unlike Pol-TPD layer, the photophysical characteristics of the NPL thin-film remain unaffected on the X-F6-TAPC layer, and further confirm the role of underneath layer on the η_{PL}. We also observed significantly short τ_{avg} of 15.95 ns (t_1 = 10.63 ns and t_2 = 29.25 ns) in the thin-film sample of LHP NPLs capped with OLA. The short lifetime in the OLA capped NPL thin-films is resulted due to dielectric quantum confinement effect and confined diffusion of free carriers.[18,19]

2.2 Optical characteristics and simulations

The refractive indices (n) of hole transporting materials, Poly-TPD and X-F6-TAPC, were estimated through fitting the non-absorbing region, 500-850 nm, of optical index data of X-F6-TAPC and Poly-TPD was fitted with the Sellmeier dispersion model. Moreover, the non-absorbing region, 550-850 nm, of optical index data of LHP NPL thin-film was fitted with the Sellmeier dispersion model. The optical constants, A_1, A_2, A_3, B_1, B_2, and B_3, of all thin films were calculated by fitting the raw data psi (ψ) and delta (Δ) plot with the SENTECH SpectraRay2 (SR2) software (Table S2). Furthermore, the analysis was completed when Tauc–Lorentz (TL) model was applied in order to account for optical absorption. A reasonable fit was obtained with two TL oscillators in the range of 500–700 nm. The Poly-TPD and X-F6-TAPC shows the refractive indices of 1.65 and 1.54, respectively, at the PL emission maxima 528 nm of LHP NPLs. Moreover, the refractive index of NPL thin-film of 1.72±0.01. We have also chosen a low refractive index electron transporting material, 3TPYMB (n = 1.66 at 528 nm).[20]

To gain more understanding, the optical simulations were performed to understand the role of hole transporting layer (HTL) and electron transporting layer thicknesses and their refractive indices on the light out-coupling efficiencies (η_{out}) in the optimal device architecture (Fig. S10). Figure S10a shows the contour plot of the η_{out} of optimal device as a function of HTL, X-F6-TAPC, and ETL, 3TPYMB, thicknesses by using the horizontally oriented (Θ_H) TDM of 1, and optimized NPL emission layer thickness. The optical simulations were performed by assuming the zero electrical loss, while the charge carrier recombination zone was assumed in the middle of the NPL thin-film emission layer. As we have not observed any noteworthy change in the η_{out} by varying the position of recombination zone in the LHP emission layer. Upon varying the layer thicknesses of low refractive index cross-linkable HTL, X-F6-TAPC (n = 1.54 at 528 nm), and ETL, 3TPYMB (n = 1.66 at 528 nm), between 5 and 200 nm, the η_{out} ranges between 2.5 and 47%. Most interestingly, the optimal LED device with an emission layer having a corresponding exciton TDM either partially, 0.72, or entirely, 1, oriented toward horizontal direction demonstrates a highest η_{out} of 32.4 and 41.15%. Our optical simulation results further affirms the significance of low refractive index carrier transporting materials, X-F6-TAPC as HTL and

3TPYMB as ETL, and horizontal orientation of exciton TDM on the η_{out} (Fig. S10b-d). Our simulations confirms that the lower and upper η_{out} greatly enhanced from 17 to 29% and 37 to 54%, respectively, as the orientation of TDM increases from 0.67 (isotropic) to 1 (completely horizontal). Particularly, the two-dimensional superlattices (2DSLs) film of LHP NPLs show a notably higher η_{out}, 19 - 39%, by replacing the high refractive index HTL and ETL (n = 2.0) with low refractive index (n = 1.4) counterparts (Fig. 10b).

3. EL characteristics

Considerable experimental efforts were made to optimize the auxiliary layers, including hole transporting layers (HTLs), electron transporting layers (ETLs), and electron injection layers (EILs). To assess the role of ETL and EIL on the EL performance, the LED devices consisting the 3TPYMB ETL and Liq EIL were fabricated. Upon replacing the conventional TPBi layer with the 3TPYMB, the device shows the maximum η_{ext} of 10.6% and η_{CE} of 46.6 cd A^{-1}, which are over 80% and 88%, respectively, higher than that of control device (Table S3). We attribute the higher efficiencies to low electron injection barrier and low refractive index, n = 1.65, that tenders a high η_{out} through increasing the exciton out-coupling to air mode. Furthermore, an optimal 3TPYMB thickness, 50 nm, possesses an adequate distance from the aluminum cathode, thus effectively suppress the surface plasmon polariton (SPP) losses.[20-22] The device performance further excelled (η_{ext} = 24.2% and η_{CE} = 101.7 cd m^{-1}) upon introducing an 18±1 nm thick cross-linkable X-F6-TAPC layer between PEDOT:PSS and perovskite emission layer. The superior device performance is attributed to following factors, including, (i) near-unity thin-film η_{PL}, (ii) highest occupied molecular orbital (HOMO) energy level (-5.63 eV) of X-F6-TAPC that reduce the hole injection barrier between PEDOT:PSS and EML thus enables an energy cascade route for hole injection[22,23], (iii) effective energy barrier to confine the injected carriers, electron and hole, within the EML due to a high LUMO energy level (-1.63 eV) in the X-F6-TAPC and a low-lying HOMO energy level (-6.8 eV) in the 3TPYMB [22-24], (iv) low refractive indices in the X-F6-TAPC (n = 1.54) HTL, perovskite EML (n = 1.73), and 3TPYMB (n = 1.66) ETL that greatly enhance the η_{out} (details see Supplementary Section 2).[20,21,25] We have also tested two other electron-transporting materials, 2,4,6-tris[3-(diphenylphosphinyl)phenyl]-1,3,5-triazine (PO-T2T) and 4,6-bis(3,5-di(pyridin-3-yl)phenyl)-2-methylpyrimidine (B3PYMPM) in the LED devices to attain better EL performance. The devices with PO-T2T as ETL demonstrate significantly lower efficiencies (η_{ext} = 10.34% and η_{CE} = 42.52 cd m^{-1}) than that of champion device, while higher efficiencies than the device consisting B3PYMPM as ETL (η_{ext} = 8.69% and η_{CE} = 36.11 cd m^{-1}). Particularly, the poor device performance in the devices with the PO-T2T and B3PYMPM ETLs than the 3TPYMB based device because of (i) large electron injection barrier due to high LUMO energy level (-2.8 eV) and relatively higher refractive index of (n = 1.74 at 528 nm) in PO-T2T, while a considerably higher refractive index (n = 1.86 at 528 nm).

These factors either significantly reduce the η_{out} by increasing the total internal reflection (TIR) or unfavorably enable a carrier injection imbalance during the device operation.[20,21] We observed the consistent EL emission maxima at 528 nm in all devices without any parasitic emission from underneath HTL, poly-TPD and X-F6-TAPC (Fig. S11).

Our champion device exhibits ultra-pure green emission chromaticity with the $CIE_{x,y}$ coordinates ranging between (0.168, 0.771) and (0.174, 0.795), which are almost identical with the standard Rec. 2020 color coordinates (0.170, 0.797). The optimal LED devices demonstrate "greenest" EL emission, to our knowledge, that covers 99.5% and 99.8% of the Rec. 2020 standard gamut area in the CIE 1931 and the CIE 1976 color space, respectively, upon substituting from the standard green chromaticity coordinates.[26,27]

As shown in Fig. S14, our optimal device exhibits a 0.73V rise in the operational voltage (ΔV), when the device stressed at a constant current density of 0.5 mA cm^{-2}. Moreover, the ΔV value in the control device also increases to 0.51V during the operational stability measurement. Generally, the increase in driving voltage is occurred to maintain the initial current density throughout the operation. The change in voltage during operational stability could be attributed to formation of resistive paths due to ion migration and perovskite emissive layer degradation under electric field. We observed tremendous spectral stability, as peak EL spectra of electrically stressed devices remain consistent with the fresh LED counterparts (Fig. S15).

Table

Table S1. Photophysical characteristics of the LHP NPLs thin films deposited on bare glass substrate and HTL, poly-TPD and X-F6-TAPC.

LHP NPLs film on	η_{PL} (%)	$\lambda_{max.}$ (nm)	fwhm (nm)	τ_{avg} (ns)	t_1 (ns)	t_2 (ns)
bare glass	98.2 ± 1.8	528.9	22.8	51.1	19.5	78.2
poly-TPD layer	45.7 ± 1.8	527.3	23.3	44.2	18.5	68.9
X-F6-TAPC layer	95.3 ± 1.3	527.4	23.2	50.0	19.2	75.8

Table S2. Sellmeier parameters obtained from fitting the SE data for anisotropically confined LHP NPLs, cross-linkable hole transporting material (HTM), X-F6-TAPC, and a conventional polymeric HTM, Poly-TPD.

Material	A_1 (-)	A_2 (-)	A_3 (-)	B_1 (μm^2)	B_2 (μm^2)	B_3 (μm^2)
LHP NPLs	1.49513	1.181517	5.38914	0.05010	30180.03125	11148.9932
X-F6-TAPC	1.29824	6412.6567	1013.648	0.05116	39260.57031	2950.19287
Poly-TPD	0.94802	0.0186308	1.610195	0.11773	30184.38281	11170.6973

Table S3. EL characteristics of perovskite quantum dot LEDs.

Device	V_{on} (V)	η_{CE} (cd A^{-1})	η_{ext} (%)	λ_{max} (nm)
ITO/PEDOT:PSS/$FA_{0.5}MA_{0.5}PbBr_3$/TPBi/LiF/Al	2.75	24.74	5.87	528
ITO/PEDOT:PSS/$FA_{0.5}MA_{0.5}PbBr_3$/3TPYMB/LiF/Al	2.75	37.86	9.44	528
ITO/PEDOT:PSS/$FA_{0.5}MA_{0.5}PbBr_3$/3TPYMB/Liq/Al	2.75	46.60	10.6	528
ITO/PEDOT:PSS/ X-F6-TAPC/$FA_{0.5}MA_{0.5}PbBr_3$/PO-T2T/Liq/Al	3.00	42.52	10.34	528
ITO/PEDOT:PSS/X-F6-TAPC/$FA_{0.5}MA_{0.5}PbBr_3$/B3PYMB/Liq/Al	3.00	36.11	8.69	528
ITO/PEDOT:PSS/X-F6-TAPC/$FA_{0.5}MA_{0.5}PbBr_3$/3TPYMB/Liq/Al	2.80	101.7	24.2	528
ITO/PEDOT:PSS/Poly-TPD/X-F6-TAPC/$FA_{0.5}MA_{0.5}PbBr_3$/ 3TPYMB/Liq/Al	3.00	35.6	8.6	528

Figures

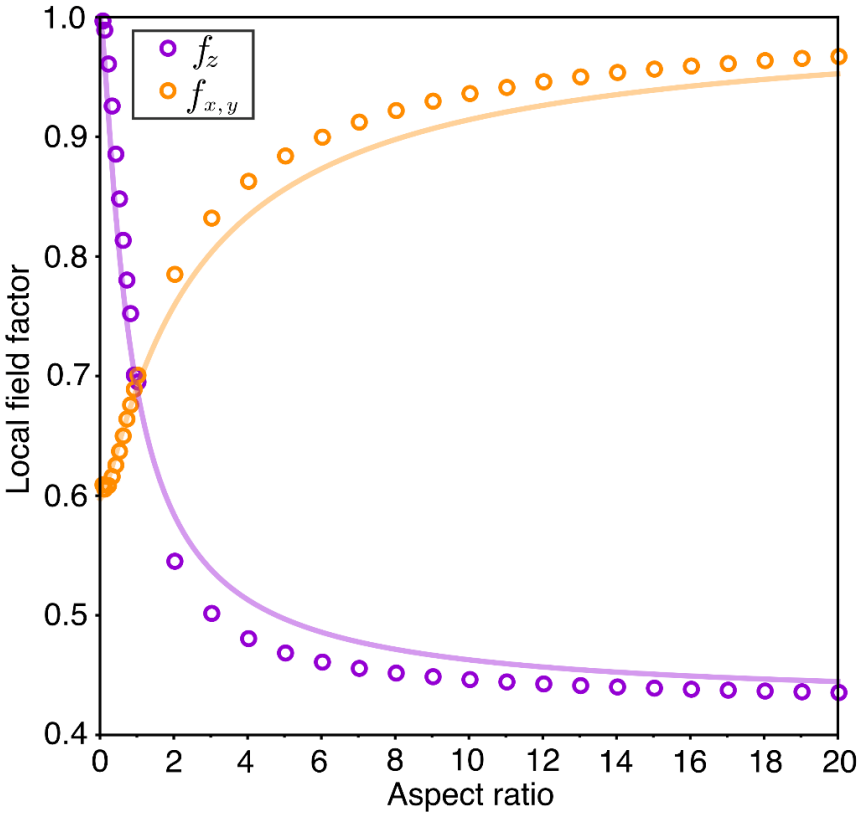

Supplementary Figure S1. Local field factors as a function of the aspect ratio. The solid lines correspond to the analytical solutions for the spheroids eq. (5), and the open circles are the numerical solutions for cuboids.

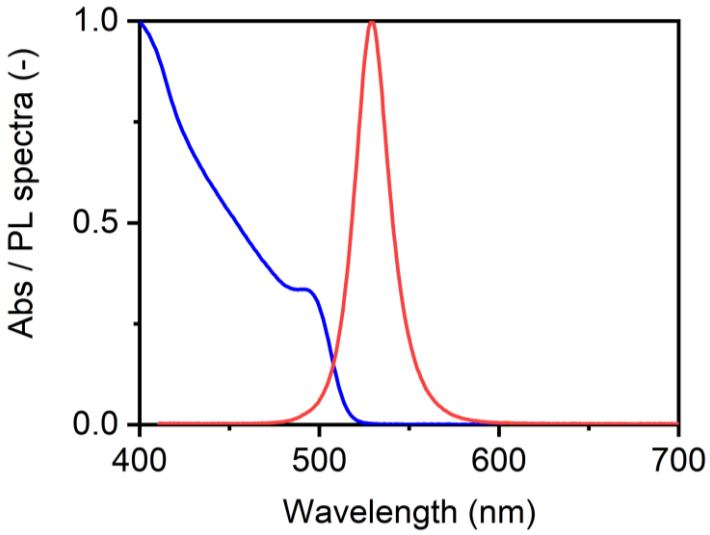

Supplementary Figure S2. The PL (red line) and absorption (Abs.; blue line) spectra of colloidal LHP NCs recorded in toluene.

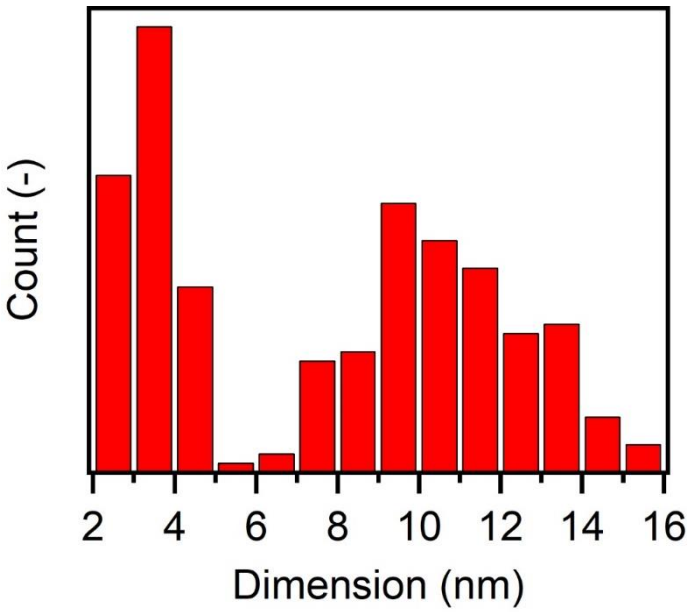

Supplementary Figure S3. Histograms of lateral size distribution by analyzing the cryo-TEM micrograph.

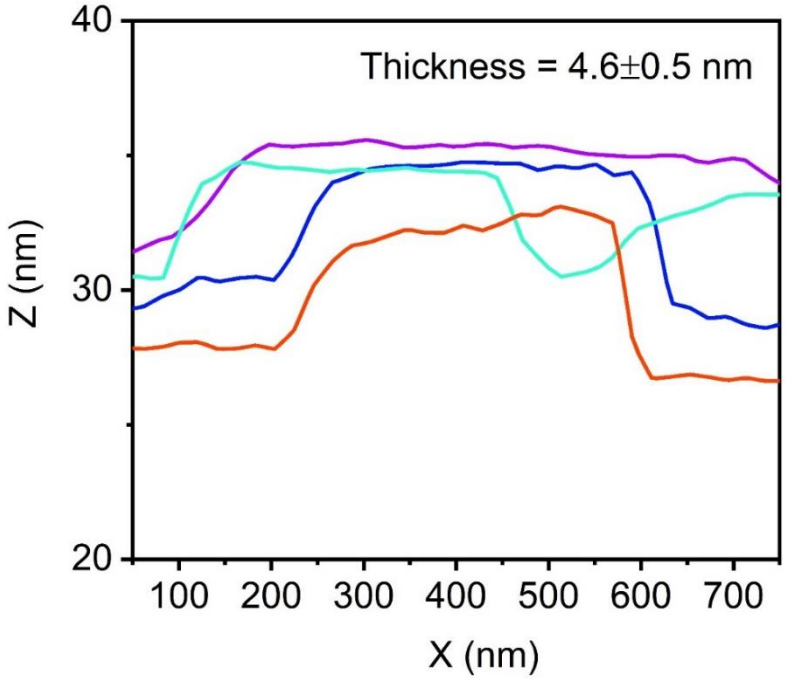

Supplementary Figure S4. Cross-sectional height profiles of 2D assembly of NPLs in the *xy* (substrate) plane, in AFM height image presented in Figure 2b.

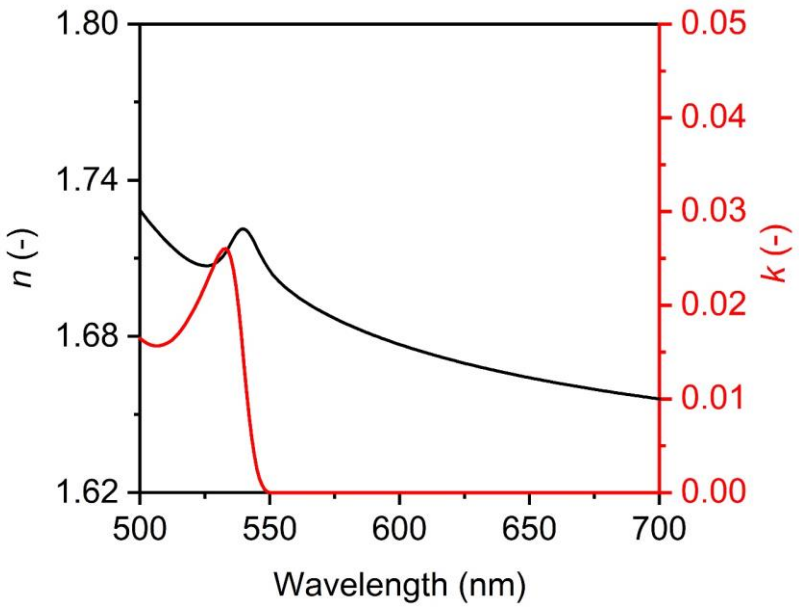

Supplementary Figure S5. Spectroscopic ellipsometry analysis of anisotropically confined LHP NCs film. The refractive index of anisotropically confined LHP NCs film were measured by fitting the spectroscopic ellipsometer amplitude components, delta (Δ) and psi (Ψ) as a function of incident light wavelength, with the Tauc-Lorentz model (left panel). As a result a relation between refractive index and wavelength was obtained (right panels). *n* and *k* stand for the real and imaginary component of the refractive index, respectively.

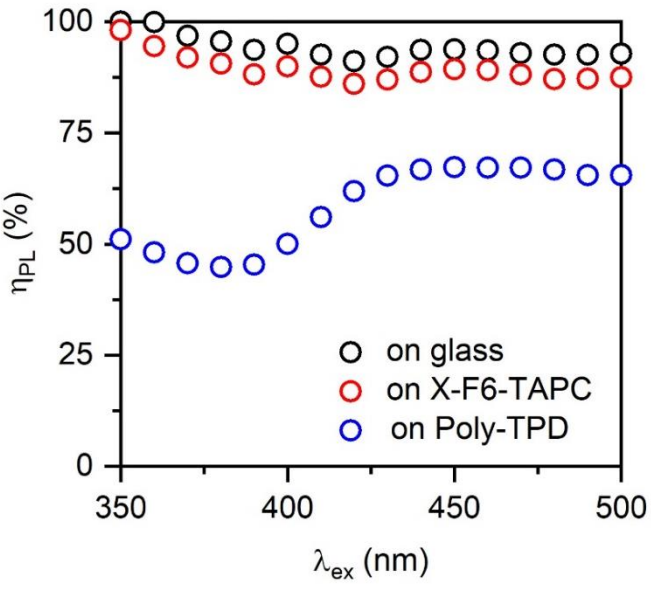

Supplementary Figure S6. The η_{PL} of anisotropically confined LHP NCs on the glass, X-F6-TAPC, and Poly-TPD thin films by varying excitation wavelengths (λ_{ext}) from 350 to 500 nm.

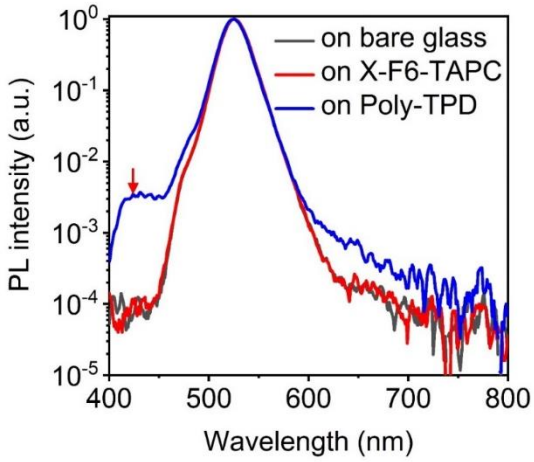

Supplementary Figure S7. PL spectra of anisotropically confined LHP NPLs solid thin films on the bare glass, X-F6-TAPC, and Poly-TPD thin films.

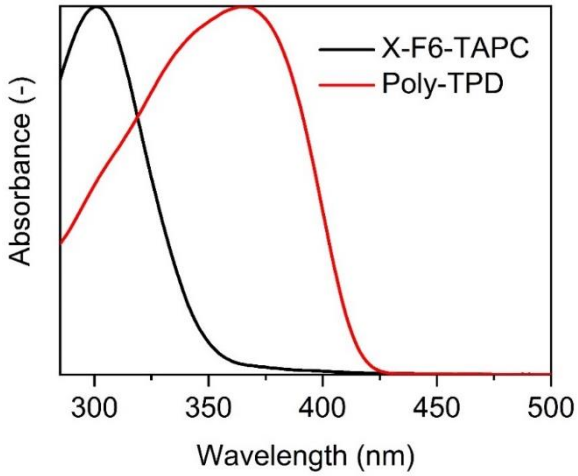

Supplementary Figure S8. Absorbance spectra of X-F6-TAPC (black line) and Poly-TPD (red line) hole transporting layers.

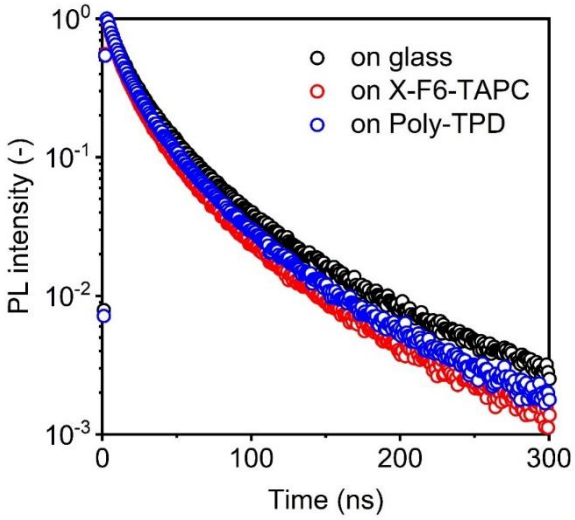

Supplementary Figure S9. Time resolved PL spectra of anisotropically confined LHP NPLs thin films on the bare glass substrate (black circle), X-F6-TAPC (red circle), and Poly-TPD (blue circle) thin films.

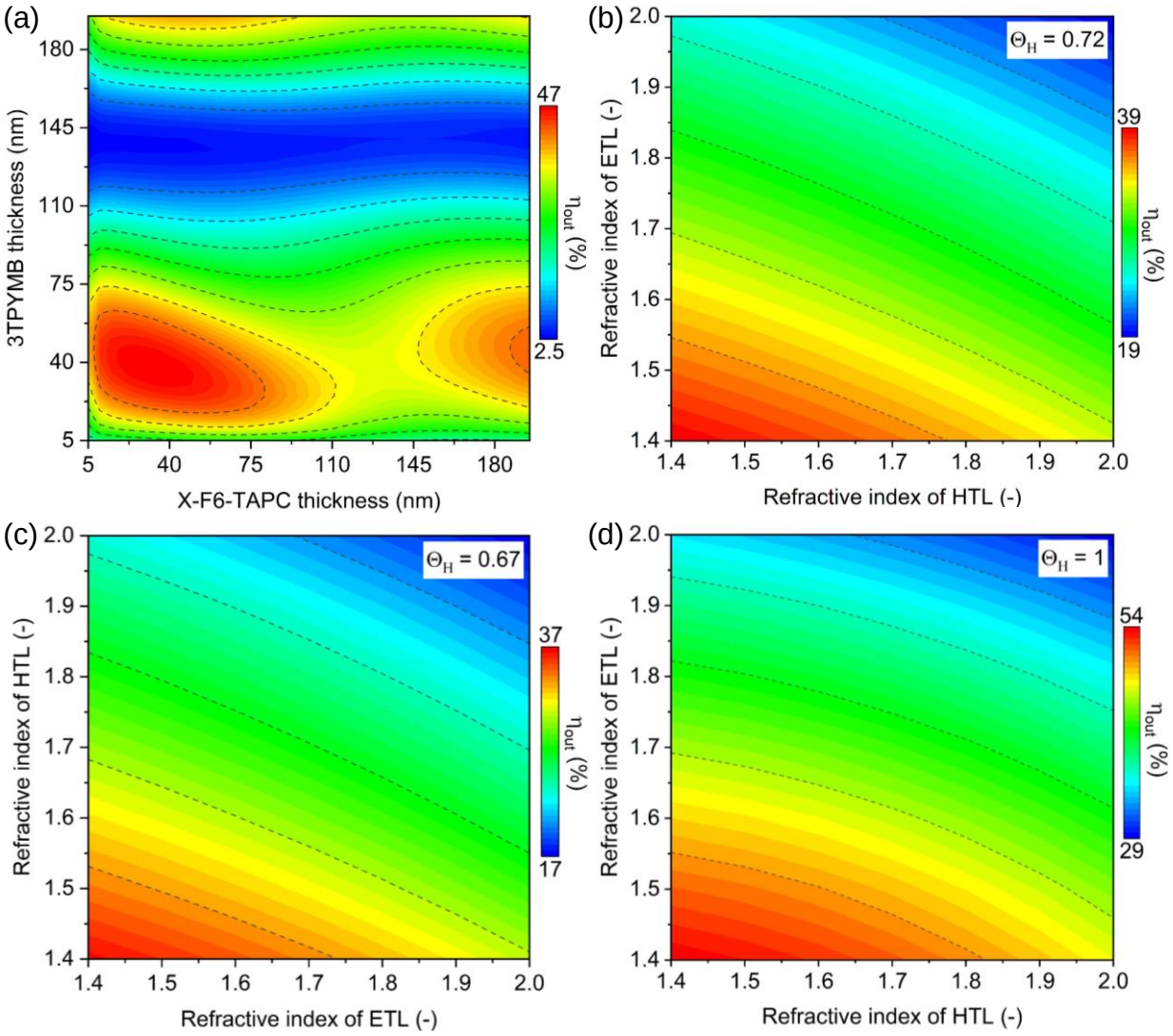

Supplementary Figure S10. a. Contour plot of maximum achievable light extraction efficiency (η_{out}) distribution as a function of electron transporting layer, 3TPYMB, and hole transporting layer, X-F6-TAPC, thicknesses. Contour plot of maximum achievable light extraction efficiency (η_{out}) distribution as a function of TDM orientation, **b.** Θ_H = 0.72 (experimental), **c.** Θ_H = 0.67 (isotropic), and **d.** Θ_H = 1 by varying the refractive indices of HTLs and ETLs between 1.4 and 2.0.

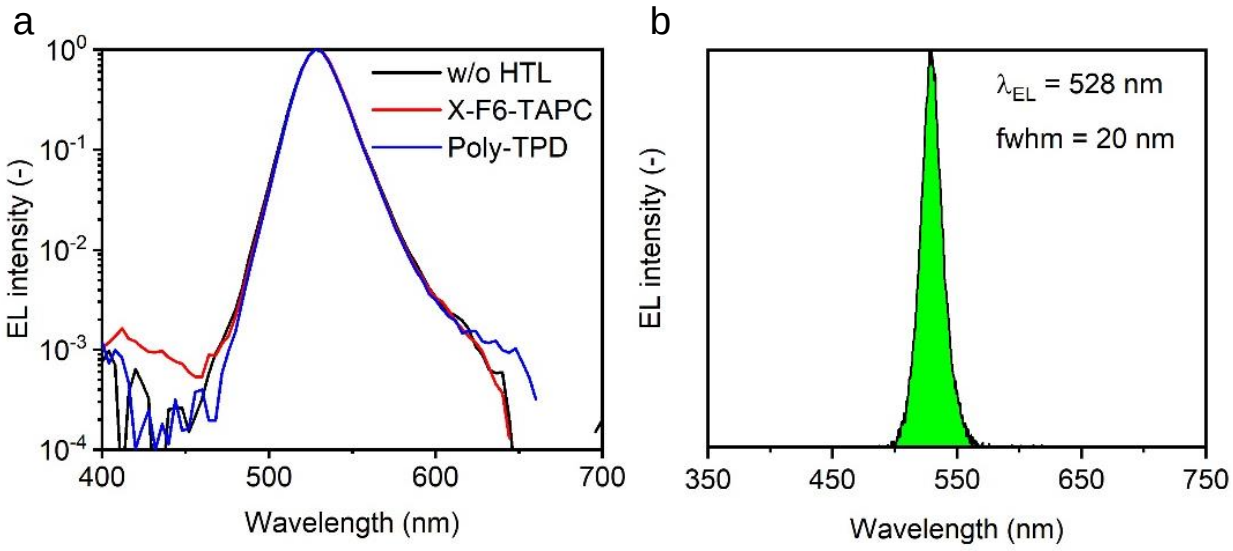

Supplementary Figure S11. a. EL spectra of devices, either without (w/o) HTL or having X-F6-TAPC, and poly-TPD as HTL. **b.** EL spectra of optimal perovskite QD LEDs demonstrating ultra-pure green emission with $CIE_{x,y}$ coordinates of (0.174, 0.795).

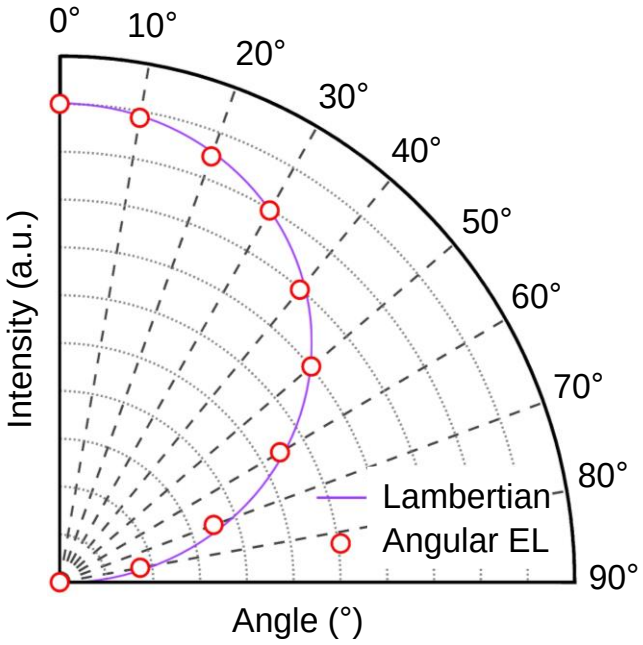

Supplementary Figure S12. Distribution of EL emission intensities of the perovskite QD LED device by varying the viewing angles between 0° and 90°.

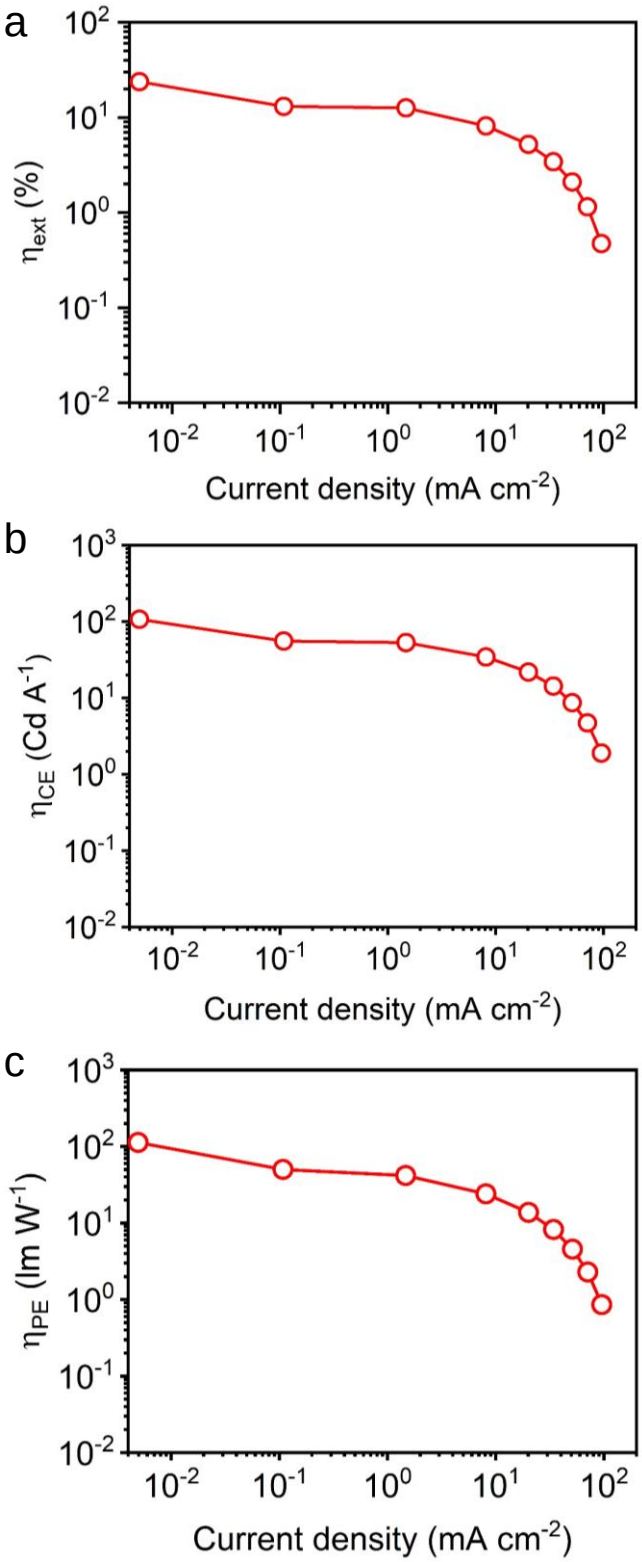

Supplementary Figure S13. EL characteristics of champion perovskite QD LED device. **a**, η_{ext} as a function of current density. **b**, η_{CE} as a function of current density. **c**, η_{PE} as a function of operation voltage.

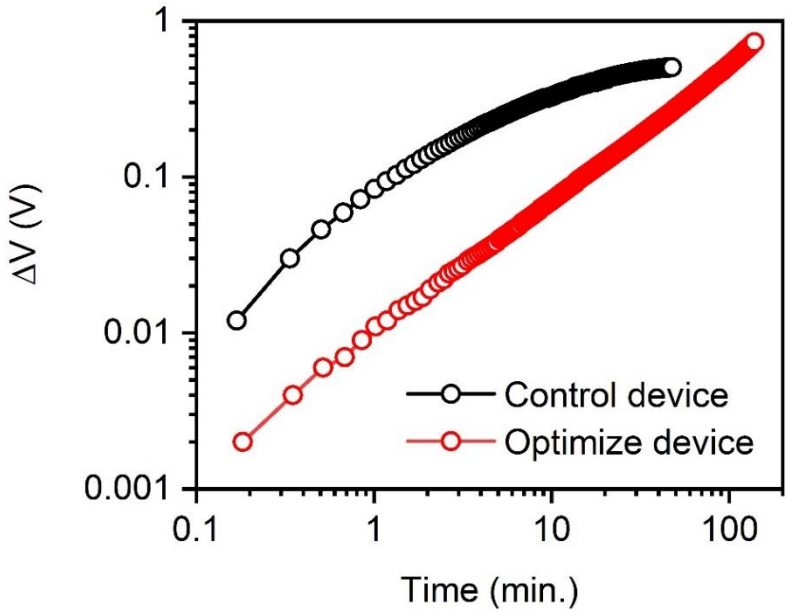

Supplementary Figure S14. Change in operating voltage (ΔV; offset to zero) in the control and optimal LED devices as a function of time under continuous electrical stress at a constant current density of 0.5 mA cm^{-2}.

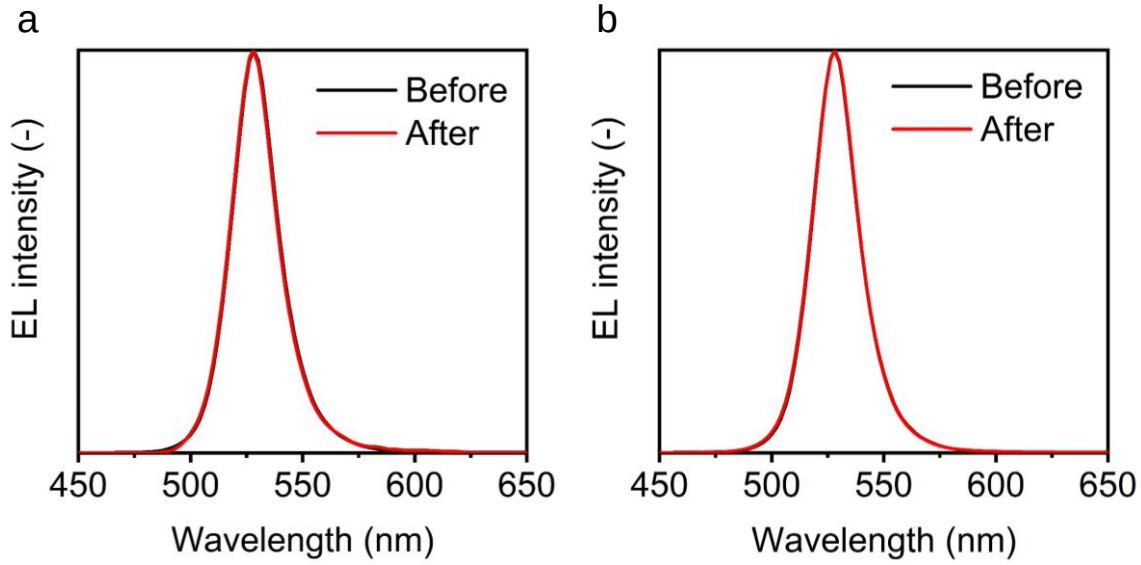

Supplementary Figure S15. EL spectra of **a,** control and **b,** optimize devices before and after operational lifetime test.

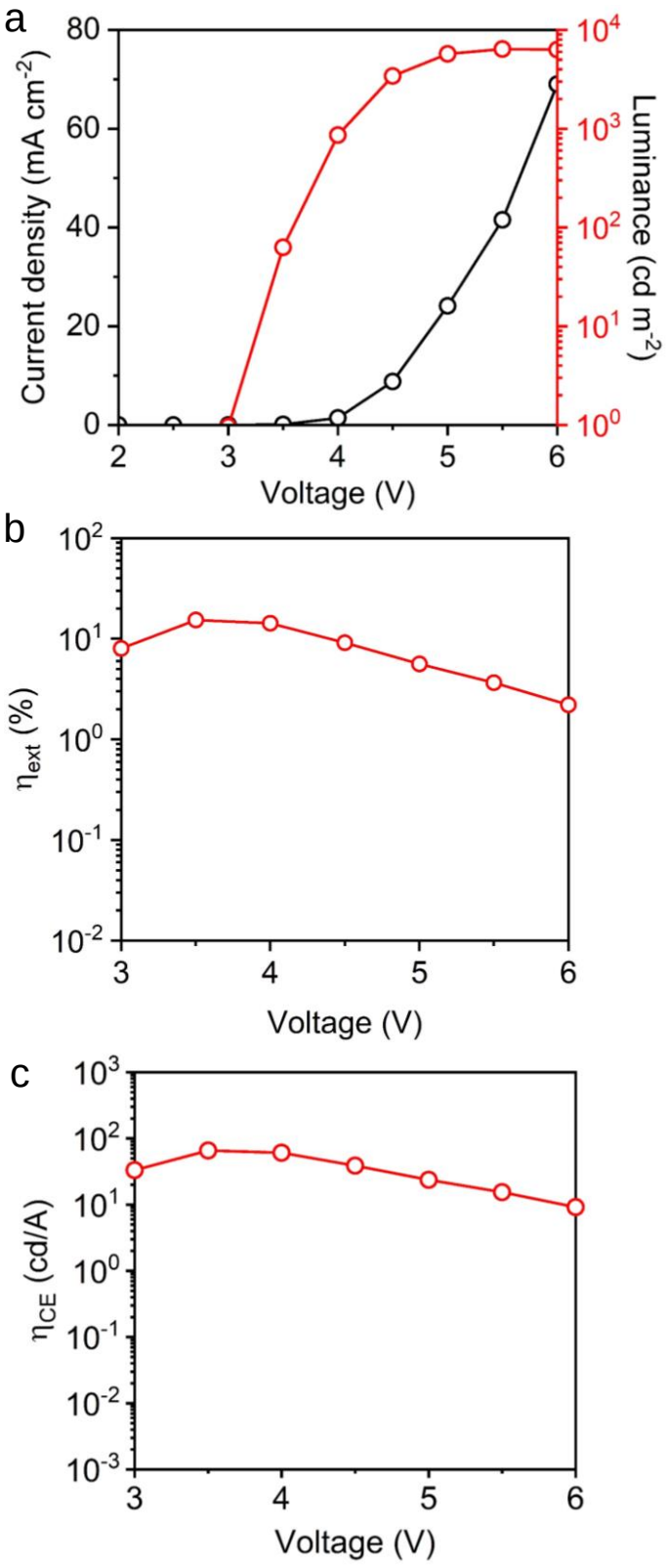

Supplementary Figure S16. EL characteristics of large area perovskite QD LED device. **a**, current density and luminance as a function of driving voltage. **b**, η_{ext} as a function of driving voltage. **c**, η_{CE} as a function of driving voltage.

References

1 Tanaka, K. *et al.* Comparative study on the excitons in lead-halide-based perovskite-type crystals $CH_3NH_3PbBr_3$ $CH_3NH_3PbI_3$. *Solid State Commun.* **127**, 619-623, (2003).

2 Grynberg, G., Aspect, A. & Fabre, C. *Introduction to Quantum Optics: From the Semi-classical Approach to Quantized Light*. (Cambridge University Press, 2010).

3 Becker, M. A. *et al.* Bright triplet excitons in caesium lead halide perovskites. *Nature* **553**, 189-193, (2018).

4 Peter Y. Yu, M. C. *Fundamental of Semiconductors*. 4th edn, (Springer, 2010).

5 Scott, R. *et al.* Directed emission of CdSe nanoplatelets originating from strongly anisotropic 2D electronic structure. *Nature Nanotechnol.* **12**, 1155-1160, (2017).

6 Markel, V. A. Introduction to the Maxwell Garnett approximation: tutorial. *J. Opt. Soc. Am. A* **33**, 1244-1256, (2016).

7 Hens, Z. & Moreels, I. Light absorption by colloidal semiconductor quantum dots. *J. Mater. Chem.* **22**, 10406-10415, (2012).

8 Bohren, C. F. & Huffman, D. R. *Absorption and Scattering of Light by Small Particles*. 1 edn, (WILEY, 1998).

9 Sihvola, A. *Electromagnetic Mixing Formulas and Applications*. 1st edn, (The Institution of Engineering and Technology, 2008).

10 Galkowski, K. *et al.* Determination of the exciton binding energy and effective masses for methylammonium and formamidinium lead tri-halide perovskite semiconductors. *Energy Environ. Sci.* **9**, 962-970, (2016).

11 Glaser, T. *et al.* Infrared spectroscopic study of vibrational modes in methylammonium lead halide perovskites. *J. Phys. Chem. Lett.* **6**, 2913-2918, (2015).

12 Sendner, M. *et al.* Optical phonons in methylammonium lead halide perovskites and implications for charge transport. *Mater. Horiz.* **3**, 613-620, (2016).

13 Ruda, H. E. & Shik, A. Polarization-sensitive optical phenomena in semiconducting and metallic nanowires. *Phys. Rev. B* **72**, 115308, (2005).

14 Sattler, K. D. *Handbook of Nanophysics: Nanoelectronics and Nanophotonics*. 1 edn, (CRC Press, 2010).

15 Jagielski, J. *et al.* Scalable photonic sources using two-dimensional lead halide perovskite superlattices. *Nat. Commun.* **11**, 387, doi:10.1038/s41467-019-14084-3 (2020).

16 Sercel, P. C., Lyons, J. L., Bernstein, N. & Efros, A. L. Quasicubic model for metal halide perovskite nanocrystals. *J. Chem. Phys.* **151**, 234106, (2019).

17 Folie, B. D. *et al.* Effect of anisotropic confinement on electronic structure and dynamics of band edge excitons in inorganic perovskite nanowires. *J. Phys. Chem. A* **124**, 1867-1876, doi:10.1021/acs.jpca.9b11981 (2020).

18 Kumar, S., Jagielski, J., Marcato, T., Solari, S. F. & Shih, C.-J. Understanding the ligand effects on photophysical, optical, and electroluminescent characteristics of hybrid lead halide perovskite nanocrystal solids. *J. Phys. Chem. Lett.* **10**, 7560-7567, (2019).

19 Shamsi, J., Urban, A. S., Imran, M., De Trizio, L. & Manna, L. Metal halide perovskite nanocrystals: synthesis, post-synthesis modifications, and their optical properties. *Chem. Rev.* **119**, 3296-3348, (2019).

20 Salehi, A. *et al.* Highly efficient organic light-emitting diode using a low refractive index electron transport layer. *Adv. Opt. Mater.* **5**, 1700197, (2017).

21 Shin, H. *et al.* Sky-Blue Phosphorescent OLEDs with 34.1% External quantum efficiency using a low refractive index electron transporting layer. *Adv. Mater.* **28**, 4920-4925, (2016).

22 Jou, J.-H., Kumar, S., Agrawal, A., Li, T.-H. & Sahoo, S. Approaches for fabricating high efficiency organic light emitting diodes. *J. Mater. Chem. C* **3**, 2974-3002, (2015).

23 Liaptsis, G. & Meerholz, K. Crosslinkable TAPC-based hole-transport materials for solution-processed organic light-emitting diodes with reduced efficiency roll-off. *Adv. Funct. Mater.* **23**, 359-365, (2013).

24 Daisaku, T., Takashi, T., Takayuki, C., Soichi, W. & Junji, K. Novel electron-transport material containing boron atom with a high triplet excited energy level. *Chem. Lett.* **36**, 262-263, doi:10.1246/cl.2007.262 (2007).

25 Umbach, T. E. *et al.* Low-refractive index layers in organic light-emitting diodes via electrospray deposition for enhanced outcoupling efficiencies. *Adv. Eng. Mater.* **22**, 1900897, (2020).

26 Kumar, S. *et al.* Ultrapure green light-emitting diodes using two-dimensional formamidinium perovskites: Achieving recommendation 2020 color coordinates. *Nano Lett.* **17**, 5277-5284, (2017).

27 Fukagawa, H., Oono, T., Iwasaki, Y., Hatakeyama, T. & Shimizu, T. High-efficiency ultrapure green organic light-emitting diodes. *Mater. Chem. Front.* **2**, 704-709, (2018).